J. Mech. Phys. Solids 146 (2021) 104203

Contents lists available at ScienceDirect

Journal of the Mechanics and Physics of Solids

journal homepage: www.elsevier.com/locate/jmps

A coupled mechano-chemical peridynamic model for pit-to-crack transition in stress-corrosion cracking

Ziguang Chen [a,b,*], Siavash Jafarzadeh [c], Jiangming Zhao [c], Florin Bobaru [c,**]

[a] Department of Engineering Mechanics, School of Aerospace Engineering, Huazhong University of Science and Technology, Wuhan 430074, China
[b] Hubei Key Laboratory of Engineering Structural Analysis and Safety Assessment, 1037 Luoyu Road, Wuhan 430074, China
[c] Department of Mechanical and Materials Engineering, University of Nebraska-Lincoln, Lincoln, NE 68588-0526, USA

A B S T R A C T

We introduce a coupled mechano-chemical peridynamic model to describe stress corrosion cracking. In this model, two mechanisms, stress-dependent anodic dissolution and diffuse corrosion layer-assisted fracture, are considered to influence pitting and crack propagation in stress corrosion cracking. Diffusion peridynamic bonds (acting as dissolution bonds at the solid/liquid interface) and mechanical peridynamic bonds are used to represent the interactions between material points. Mechanical bonds can be damaged by mechanical stretching or by anodic dissolution. The magnitude of the dissolution fluxes for diffusion peridynamic bonds depends on both mechanical deformation and the applied electrical potential. The coupling between anodic dissolution and mechanical damage leads to cracks that initiate in the corrosion damage layer and propagate into the bulk. A 2D three-point bending/corrosion test demonstrates the concept. We verify the model in 3D using an experimental test from the literature for the case of stress-corrosion cracking process in a steam turbine steel sample. The model's results capture the pit-to-crack transition time, the pit size and shape at fracture, as well as the morphology of cracks that spring from, and connect the pits.

1. Introduction

Corrosion can cause mechanical damage near the material surface and reduce material's strength significantly (Li et al., 2018) . When corroding structures are subject to mechanical loadings, they can undergo stress corrosion cracking (SCC), which is cracking in the presence of corrosion (Cramer and Covino, 2003). Catastrophic failure can ensue, sometimes with little warning, as drastic reductions in ductility lead to quasi-brittle fracture events in materials thought to have higher toughness. The ability to simulate corrosion damage evolution and transition from pitting to crack initiation and propagation is essential for predicting residual service life of engineering structures, reliability analysis, and corrosion-resistant design of materials. The goal of this paper is to introduce a new peridynamic (PD) model for SCC and apply it to study pit-to-crack transition problems.

Pit-to-crack transition in stress-corrosion cracking has been an active research topic for the last decade. Advanced techniques, such as X-ray computed tomography (Connolly et al., 2006) and SEM (or FIB-SEM) (Hinds et al., 2013), were applied to study the pit/crack morphology, post SCC. These techniques combined with FE analysis have provided some useful insights with respect to the pit-to-crack transition (Horner et al., 2011; Zhu et al., 2013). An interesting phenomenon, revealed by three-dimensional (3D) imaging (Connolly et al., 2006), is that the pit-to-crack transition does not occur necessarily at the pit base. In SCC of a steam turbine disc steel (Connolly et al., 2006), researchers noticed that cracks did not necessarily initiate from the bottom of the pits. Similarly observed in (Zhu et al., 2013), the preferential SCC initiation sites for stainless steel are at the shoulders, rather than at the bottoms of the surface pits/defects.

* Corresponding author at: Department of Engineering Mechanics, School of Aerospace Engineering, Huazhong University of Science and Technology, Wuhan 430074, China.
** Corresponding author
E-mail addresses: zchen@hust.edu.cn (Z. Chen), fbobaru2@unl.edu (F. Bobaru).

https://doi.org/10.1016/j.jmps.2020.104203
Received 27 July 2020; Received in revised form 23 October 2020; Accepted 24 October 2020
Available online 27 October 2020
0022-5096/

The off-base locations of the cracks from pits are puzzling, given that the pits bottoms are the areas with largest stress-concentration factors, based on geometry. Traditionally, a crack was assumed to initiate from a pit when two criteria were satisfied: the pit depth exceeded a threshold value and the crack growth rate was greater than the pit growth rate (Kondo, 1989; Turnbull et al., 2010). The first criterion leads to crack initiating from pit bottom. Given the discrepancy between experimental observations and this traditional point of view, a new mechanism needs to be introduced and corresponding models have to be implemented for a better understanding of SCC.

Most of the numerical models used for SCC, such as cohesive zone model (Xiang et al., 2019) and phase field model (Nguyen et al., 2018), generate cracks that grow from the base of pits in systems under mechanical loadings. The reason for the models' inability to capture cracks initiating from pit locations other than the lowest point on the pit bottom, is the uniformity of corrosion front that they produce. In reality, the corrosion damage layer (Chen and Bobaru, 2015a; Jafarzadeh et al., 2019a; Li et al., 2018; Li et al., 2016) is highly non-uniform, with even mechanical properties changing, stochastically, through its thickness (Li et al., 2018; Li et al., 2016; Vallabhaneni et al., 2018; Yavas et al., 2018). Computational models that simulate corrosion as a diffusion process in the electrolyte and consider the motion of the corrosion front a moving-boundary problem, cannot capture this behavior. Models like those in (Chen and Bobaru, 2015a; Jafarzadeh et al., 2018b; Jafarzadeh et al., 2019a; Jafarzadeh et al., 2019c), which view the corrosion process as affecting the solid material through a certain thickness, effectively coupling diffusion in electrolyte with dissolution and mechanical damage at the corrosion layer, allow for the potential of cracks initiating from locations other than the bottom of a pit (Li et al., 2018).

In summary, a potentially successful model for pit-to-crack transition needs to be autonomous (to allow for unrestricted evolution of the corrosion front), and stochastic (to permit heterogeneities in the corrosion damage layer). Finite volume approaches (Scheiner and Hellmich, 2007, 2009), cellular automata (CA) models (Di Caprio et al., 2011; Malki and Baroux, 2005; Pérez-Brokate et al., 2016; Rusyn et al., 2015; Stafiej et al., 2013; Van der Weeën et al., 2014), peridynamic (PD) models (Chen and Bobaru, 2015a; Chen et al., 2016a; De Meo and Oterkus, 2017; Jafarzadeh et al., 2018a; Jafarzadeh et al., 2018b; Jafarzadeh et al., 2019a) and phase-field models (Ansari et al., 2018; Chadwick et al., 2018; Mai and Soghrati, 2018; Mai et al., 2016; Nguyen et al., 2018; Tsuyuki et al., 2018) are the main methods used recently in modeling pitting corrosion. A detailed recent review of corrosion damage models is presented in (Jafarzadeh et al., 2019b). Among these models, only CA and PD models generate structural heterogeneities at the corrosion fronts. In CA simulations, reaction-based transition rules of the discrete cell states are a convenient tool to sometimes obtain realistic-looking and stochastic pit morphologies. However, the major drawback of this approach is that the time magnitude and spatial sizes (model's physical dimensions) are not physical quantities, and need to be calibrated for particular transition rules and particular experimental observations (Van der Weeën et al., 2014).

Peridynamics, a new non-local model, has been proposed originally for fracture problems by Silling in Silling (2000). The governing equations in PD are in the form of integro-differential equations instead of the partial differential equations (PDEs) arising from classical, local models. Spatial gradients at each material point in the classical models are replaced by integrals of interactions of that point with its family of points. The advantage of replacing spatial derivatives with integrals is the elimination of smoothness requirements for the unknown field. This formulation is particularly useful in handling evolving discontinuities, such as propagating cracks in a solid (Zhang et al., 2016). Using this method, promising results have been obtained in, for example, dynamic brittle fracture in glass (Ha and Bobaru, 2011; Hu et al., 2013), fiber-reinforced composites (Hu et al., 2012; Mehrmashhadi et al., 2019). The model has been extended to diffusion-type problems (Bobaru and Duangpanya, 2010, 2012; Chen and Bobaru, 2015b), and, in particular, to modeling corrosion damage (Chen and Bobaru, 2015a; Jafarzadeh et al., 2018b; Jafarzadeh et al., 2019a).

The basic difference between classical models (which model corrosion as a diffusion problem in the electrolyte domain only, with a moving boundary) and peridynamic models for corrosion is that in peridynamics, corrosion is viewed as a type of damage induced in the solid by the dissolution process, coupled with the diffusion problem in the electrolyte. The benefit of such an approach can be far-reaching because it can capture important changes that happen in the solid phase, near the corrosion front, leading to a better understanding of the factors that control the loss of ductility observed in corroded samples (Li et al., 2018; Liu et al., 2008; Song et al., 2005). The peridynamic model for corrosion damage couples diffusion of metal ions in the electrolyte, phase-change due to dissolution at the corrosion front, and mechanical damage in the corroding layer, offering a more complete description of corrosion damage (Chen and Bobaru, 2015a). Moreover, the stochastic damage layer, seamlessly attached to the bulk, mimics the real case scenario in which cracks may initiate at other points than the deepest point in a pit (Li et al., 2018).

In this paper, we extend a stress-dependent corrosion PD model recently published in Jafarzadeh et al. (2019c) to consider mechanical damage produced not only by the corrosion process, via anodic dissolution, but also by mechanical strains. This extended PD model is applied to study the pit-to-crack transition. The paper is organized as follows: In Section 2 we present brief reviews of peridynamics and of the peridynamic corrosion model, together with the main algorithm for the coupled corrosion-fracture model. In Section 3, we apply the coupled model for a 2D SCC problem in a corroding metal beam under three-point bending condition, and show how the SSC process, as a combination of anodic dissolution and mechanical damage, leads to progressive material failure. In Section 4, we validate the model by comparing the pit/crack morphology and cracking initiation time against some experimental measurements from the literature. We present our conclusions in Section 5.

2. Peridynamic corrosion-fracture model

The peridynamic (PD) theory, introduced by Silling (2000) as a reformulation of the classical continuum mechanics, is an integral-type nonlocal model that allows fracture and damage to be treated as natural parts of the solution process. In the PD theory, the interaction between a material point $\boldsymbol{x}$(see Fig. 1) and its neighbors extends beyond the nearest neighbors, over a region called the "horizon" (H_x). The radius of this neighborhood is denoted by $\delta$and is called the *horizon size (or in short, the "horizon", when there is no*

danger of confusion with the horizon region). Material points in the horizon neighborhood of $\boldsymbol{x}$, are called the family of $\boldsymbol{x}$and are generically denoted by $\widehat{\boldsymbol{x}}$(see Fig. 1). Line segments in Fig. 1represent PD bonds, transferring the pair-wise information between points. In elasticity, for instance, bonds are similar to springs exerting forces between points in a family (Silling, 2000). For diffusion problems (e.g. heat and mass transfer), bonds are similar to conductors (or pipes) that carry heat (or mass) from one point to another (Bobaru and Duangpanya, 2010). In this study, PD bonds used in the formulation for material deformation or damage are called "mechanical bonds", while bonds carrying mass (concentration) information are referred to as "diffusion bonds". Before we introduce the peridynamic coupling among elasticity, corrosion, and damage for SCC modeling, we briefly review the peridynamic models for elasticity and fracture, and corrosion damage in the next two sections, respectively.

2.1. Peridynamic fracture model

Peridynamics, originally as a reformulation of the classical continuum mechanics, allows for a natural treatment of discontinuities in materials by employing the concept of nonlocal interactions. It has been successfully applied to deal with cracks and damage in solid mechanics especially in situations where the crack path is not known in advance (Bobaru et al., 2016; Cheng et al., 2020; Ha and Bobaru, 2011; Hu et al., 2012). The PD equations of motion at a point $\boldsymbol{x}$and time $t$are (Silling, 2000):

$$\rho(\boldsymbol{x},t)\ddot{\boldsymbol{u}}(\boldsymbol{x},t)=\int_{H_x}\boldsymbol{f}(\widehat{\boldsymbol{x}}-\boldsymbol{x},\boldsymbol{u}(\widehat{\boldsymbol{x}},t)-\boldsymbol{u}(\boldsymbol{x},t))\mathrm{d}V_{\widehat{\boldsymbol{x}}}+\boldsymbol{b}(\boldsymbol{x},t) \tag{1}$$

where $\rho$is the mass density, $\boldsymbol{u}$is the displacement vector field, $H_x$is the neighborhood region of $\boldsymbol{x}$(called the horizon region, or simply the horizon), $\boldsymbol{f}$is the pair-wise force function in the peridynamic bond connecting material points $\widehat{\boldsymbol{x}}$and $\boldsymbol{x}$, and $\boldsymbol{b}$is the body force density. For a static problem, the left side of the equation vanishes, which leads to

$$\int_{H_x}\boldsymbol{f}(\widehat{\boldsymbol{x}}-\boldsymbol{x},\boldsymbol{u}(\widehat{\boldsymbol{x}})-\boldsymbol{u}(\boldsymbol{x}))\mathrm{d}V_{\widehat{\boldsymbol{x}}}+\boldsymbol{b}(\boldsymbol{x})=0. \tag{2}$$

We denote $\boldsymbol{\xi}=\widehat{\boldsymbol{x}}-\boldsymbol{x}$as the relative reference position between nodes $\boldsymbol{x}$and $\widehat{\boldsymbol{x}}$, and by $\boldsymbol{\eta}=\boldsymbol{u}(\widehat{\boldsymbol{x}},t)-\boldsymbol{u}(\boldsymbol{x},t)$, the relative displacement vector. For a horizon region with spherical symmetry, each material point has an associated horizon size (δ, the radius of the horizon region), such that

$$\boldsymbol{f}(\boldsymbol{\xi},\boldsymbol{\eta})=0 \ \textit{if} \ |\boldsymbol{\xi}|>\delta. \tag{3}$$

The force density function for a linear microelastic material is given as (Silling, 2000):

$$\boldsymbol{f}(\boldsymbol{\xi},\boldsymbol{\eta})=\frac{\boldsymbol{\xi}+\boldsymbol{\eta}}{\boldsymbol{\xi}+\boldsymbol{\eta}}c(\boldsymbol{\xi})s, \tag{4}$$

where $c(\boldsymbol{\xi})$is the micro-modulus function of the bond. The micro-modulus function can take different forms, depending on the required horizon-scale behavior (Chen et al., 2016b). Here we only consider the constant-profile micro-modulus function (independent of the bond length), which, when we setup a match of the strain energy density with the classical theory for a homogeneous deformation, leads to the following forms:

$$c(\boldsymbol{\xi})=\frac{12E}{\pi\delta^4} \tag{5}$$

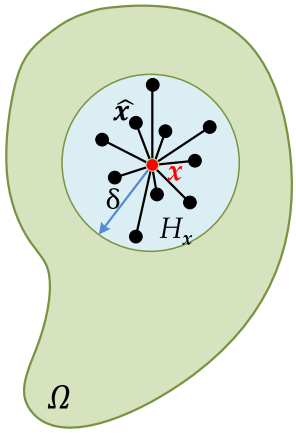

Fig. 1. Schematic of a peridynamic body Ω, and the nonlocal interactions between a material point and points in its horizon neighborhood (H_x).

in 3D [4], and

$$c(\boldsymbol{\xi}) = \begin{cases} \dfrac{9E}{\pi\delta^3}, & \text{plane stress} \\ \dfrac{48E}{5\pi\delta^3}, & \text{plane strain} \end{cases}, \tag{6}$$

in 2D. Here $E$is the Young's modulus.

The peridynamic bonds can break irreversibly, or reversibly when they are meant to represent, for example, van der Waals-like interactions (Silling and Bobaru, 2005). For irreversible bond breaking, we have $f(\boldsymbol{\xi}, \boldsymbol{\eta}) = 0, \text{ if } s > s_0$, where $s_0$is the critical bond strain, calibrated to the material's fracture energy, for the micromodulus functions given above, as follows:

$$s_0 = \sqrt{\frac{5G_0}{6E\delta}}, \tag{7}$$

in 3D, and

$$s_0 = \begin{cases} \sqrt{\dfrac{4\pi G_0}{9E\delta}}, & \text{plane stress} \\ \sqrt{\dfrac{5\pi G_0}{12E\delta}}, & \text{plane strain} \end{cases}, \tag{8}$$

in 2D. Here $G_0$is the fracture energy (energy per unit fractured area for complete separation of the body in two halves).

In uniform, or close-to-uniform discretization of the peridynamic equations, the damage index at a node is defined as the ratio between the number of broken (or failed) mechanical bonds (N_f) and the total number of bonds (N) originally associated with this node ($d(\boldsymbol{x}, t) = \frac{N_f}{N}$). Ref. Jafarzadeh et al.(2019c) considered only corrosion damage, while damage induced by mechanical loading (bond breaking due to its strain exceeding a critical value) was not included.

The type of corrosion-fracture problems we consider here feature a large time-scale separation between the corrosion and brittle fracture processes: corrosion is slow compared to crack growth. A staggered coupling model (solve a transient corrosion problem until fracture initiates, then run the fracture module until cracks arrest, before continuing with another transient solution of the corrosion problem) is warranted. Moreover, inertial effects are likely minor and the mechanical simulations performed in this work can be approximated as quasi-static. The energy minimization method is used to solve the PD elastic-brittle fracture quasi-static problem, and the nonlinear conjugate gradient method with secant line search is adopted to minimize the strain energy of the system. The details of this method can be found in Zhang et al. (2016).

2.2. Peridynamic corrosion model

Corrosion in peridynamic model is treated as a dissolution-diffusion process. Peridynamic formulations for diffusion-type problems have been introduced with the purpose to address, for example, heat and mass transfer in bodies with evolving discontinuities (Bobaru and Duangpanya, 2010, 2012). The PD equations for mass transfer, without sources or sinks are (Bobaru and Duangpanya, 2010, 2012; Chen and Bobaru, 2015b):

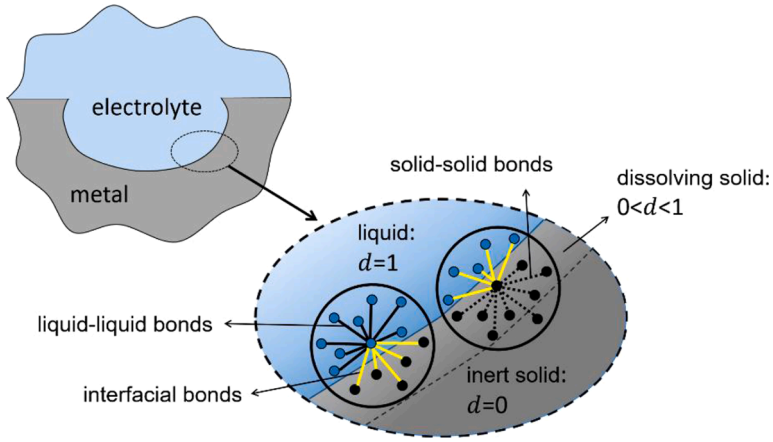

Fig. 2. Schematic of the domains and bonds defined in the PD corrosion model.

$$\frac{\partial C(\boldsymbol{x},t)}{\partial t}=\int_{H_x} k(\boldsymbol{x},\ \widehat{\boldsymbol{x}})\frac{C(\widehat{\boldsymbol{x}},\ t)-C(\boldsymbol{x},\ t)}{\widehat{\boldsymbol{x}}-\boldsymbol{x}^2}dV_{\widehat{x}}. \tag{9}$$

In Eq. (9), $C(\boldsymbol{x},t)$is the concentration at point $\boldsymbol{x}$and time t. $k(\boldsymbol{x},\ \widehat{\boldsymbol{x}})$is the micro-diffusivity of $(\boldsymbol{x},\ \widehat{\boldsymbol{x}})$ diffusion bond (see Fig. 2, different domains and the different types of bonds near the dissolution front), and it is defined as a function of mechanical damage $d(\boldsymbol{x},\ t)$(Jafarzadeh et al., 2018b; Jafarzadeh et al., 2019a):

$$k(\boldsymbol{x},\ \widehat{\boldsymbol{x}})=\begin{cases} k_{\mathrm{L}}(D), & d(\boldsymbol{x},t)=1\ \&\ d(\widehat{\boldsymbol{x}},t)=1 \\ 0, & d(\boldsymbol{x},t)<1\ \&\ d(\widehat{\boldsymbol{x}},t)<1 \\ k_{\mathrm{diss}}, & [d(\boldsymbol{x},t)\ \text{or}\ d(\widehat{\boldsymbol{x}},t)]\langle 1\ \&\ [d(\boldsymbol{x},t)\ \text{or}\ d(\widehat{\boldsymbol{x}},t)]=1 \end{cases} \tag{10}$$

$k_{\mathrm{L}}(D)$is the liquid micro-diffusivity, calculated based on the diffusivity of the electrolyte, D[56, 57]:

$$k_{\mathrm{L}}(D)=\begin{cases} \dfrac{4D}{\pi\delta^2}, & \text{in 2D} \\ \dfrac{9D}{2\pi\delta^3}, & \text{in 3D} \end{cases} \tag{11}$$

Note that different kernels can be used in Eqs. (1) and (9), which result in different forms for the micro-modulus in Eqs. (5) and (6), and for micro-diffusivity in Eq. (11) (Chen and Bobaru, 2015b; Chen et al., 2016b). Eq. (10) states that no diffusion takes place if both points belong to the solid phase. However, if one point is solid and the other point is liquid, the bond is an interfacial bond that carries the anodic dissolution micro-flux. For such bonds, $k=k_{\mathrm{diss}}$is called the micro-dissolvability (Jafarzadeh et al., 2018b; Jafarzadeh et al., 2019a).

While Eq. (9) models mass transfer via anodic dissolution at the interface and diffusion in the electrolyte, a concentration-dependent damage model, describes the evolution of the connection between damage and concentration drop during the corrosion process (Chen and Bobaru, 2015a):

$$d(\boldsymbol{x},t)=\begin{cases} 1 & ,\ C(\boldsymbol{x},t)\le C_{\mathrm{sat}} \\ \dfrac{C_{\mathrm{solid}}-C(\boldsymbol{x},t)}{C_{\mathrm{solid}}-C_{\mathrm{sat}}} & ,\ C_{\mathrm{sat}}<C(\boldsymbol{x},t)<C_{\mathrm{solid}} \\ 0 & ,\ C(\boldsymbol{x},t)=C_{\mathrm{solid}} \end{cases} \tag{12}$$

Eq. (12) implies that when concentration in the solid drops below the saturation concentration of metal ions in the electrolyte (C_{sat}) by dissolution, the solid phase changes to liquid (we set $d=1$). The damage for intact solid (full-concentration of C_{solid}) is zero. In this model, the solid region within the δdistance of the metal/electrolyte is the dissolving region (see Fig. 2) and possesses a concentration value between $C_{\mathrm{sat}}$and C_{solid}. Eq. (12)provides a relationship that determines the damage for this region according to the concentration. This partially damaged dissolving solid region with the gradual change in concentration, is in fact, the diffuse corrosion layer (Li et al., 2016) observed experimentally near the corrosion front, where, over a thickness of several micrometers, gradual changes in composition and degraded mechanical properties take place (Badwe et al., 2018; Li et al., 2018; Li et al., 2016; Vallabhaneni et al., 2018; Yavas et al., 2018).

The concentration-dependent damage in Eq. (12) translates into mechanical damage by removing mechanical bonds in the corroded region. The removal process involves a stochastic procedure described in detail in Chen and Bobaru (2015a).

The effect of stress on corrosion rate can differ among corrosion systems and different loading conditions. Elastic and plastic strains, compressive or tensile, can affect any of the chemical reactions (anodic, cathodic, passivation, etc.) present during the corrosion process. Nearly all experimental investigations suggest that tensile elastic stress is likely to increase the anodic dissolution rate. This behavior is usually explained via a mechano-chemical theory (see e.g. Gutman, 1994). We use the following constitutive relationship for k_{diss}in the stress-assisted corrosion PD model for the elastic deformation regime (Jafarzadeh et al., 2019c):

$$k^{s}_{\mathrm{diss}}(\boldsymbol{x}_L,\boldsymbol{x}_S)=k^{u}_{\mathrm{diss}}\exp[\gamma\theta(\boldsymbol{x}_S)], \tag{13}$$

where $\boldsymbol{x}_L$and $\boldsymbol{x}_S$are respectively the liquid end and the solid end of the interfacial bond, $k^{s}_{\mathrm{diss}}$is the micro-dissolvality for the stressed material, $k^{u}_{\mathrm{diss}}$is the micro-dissolvability for the unstressed material and is calibrated to the anodic current density. Parameter γ determines the stress dependency of anodic dissolution. This equation, derived from Gutman's theory (Gutman, 1994), expresses that the micro-dissolvability of an interfacial bond is exponentially related to dilatation of the solid end of that bond. The nonlocal dilatation for a bond-based material in 3D is (Zhang et al., 2016):

$$\theta(\boldsymbol{x})=3\frac{\int_{H_x}\|\ \widehat{\boldsymbol{y}}-\boldsymbol{y}\ \|-\|\ \widehat{\boldsymbol{x}}-\boldsymbol{x}\ \|\mathrm{d}V_{\widehat{x}}}{\int_{H_x}\|\ \widehat{\boldsymbol{x}}-\boldsymbol{x}\ \|\mathrm{d}V_{\widehat{x}}}. \tag{14}$$

Nonlocal dilatation is three times the average extension of mechanical bonds, and is analogous to volumetric strain in the local theory (which is three times the mean strain). In 2D, an alternative formula can be used to approximate dilatation, and the corresponding reduced micro-dissolvability is:

$$k^{s}_{\text{diss}}(\boldsymbol{x}_L, \boldsymbol{x}_S) = k^{u}_{\text{diss}} \exp\{\gamma a[s_{\max}(\boldsymbol{x}_S) + s_{\min}(\boldsymbol{x}_S)]\}. \tag{15}$$

$s_{\max}$ and $s_{\min}$ are respectively the maximum and the minimum bond-strains among the mechanical bonds connected to the point $\boldsymbol{x}_S$. For small deformation problems, a is a constant equal to 1 for plane strain and to 1/2 for plane stress conditions (see Jafarzadeh et al., 2019c).

2.3. A coupled peridynamic corrosion-fracture model

In this section, we introduce the coupled mechano-chemical peridynamic model for SCC, under the assumption of small deformations. In the previous sections, we have briefly reviewed the fracture model and the PD corrosion damage model. In the fracture model, nodes carry displacement ($\boldsymbol{u}$) and mechanical strain-induced damage index (d_s) information; in the corrosion model, nodes carry concentration (C) and corrosion-induced damage index (d_c) information. In Fig. 3, we summarize the interplay among corrosion evolution, mechanical damage, and elastic deformation.

Starting the top in Fig. 3, and going in a clockwise direction we have: corrosion dissolution induces mechanical damage (material degrades) near the corrosion front (see the corrosion-dependent damage relationship in Eq. (12)); when the damage-index is updated, at the current mechanical load, displacements (and bond strains) are solved for and updated according to Eq. (2); According to the stress/corrosion relationship in Eq. (15), we can then update the corrosion rate (micro-dissolvability). At this point we turn and read the interactions in Fig. 3 in the counter-clockwise direction. The evolution of the corrosion process leads to the corrosion front moving into the solid (solid nodes change phase to liquid nodes, according to Eq. (10)), which further changes the displacement profile at a fixed mechanical load. When the bond stretch exceeds the critical bond strain, mechanical damage occurs. The accumulated mechanical damage then advances corrosion process, according to the damage-dependent corrosion relationship in Eq. (10).

To simulate stress-corrosion cracking numerically for arbitrary geometries and boundary conditions, we use the algorithm shown in Fig. 4. This algorithm is similar to the one reported in Jafarzadeh et al. (2019c), but a major difference is that mechanical load can now induce damage, which was not considered in Jafarzadeh et al. (2019c).

The region defining the material, including both the solid and liquid phase, is discretized with a uniform grid and nodes are centered in the middle of each cell. This amounts to using a one-point Gaussian quadrature over the domain. Details for discretizing the model's equations and on the particular numerical methods used are given in Jafarzadeh et al. (2019c).

In this work, for simplicity, we use the same horizon (and discretization grid) for both the peridynamic corrosion model and peridynamic fracture model. We select the horizon size to be in the same range as the length scale of the initial micro-pits used in the examples shown below. While we calibrate the critical bond strain to the material's fracture toughness (via Eqs. (7) and (8)), for the linear-brittle fracture model employed here, the horizon size introduces a certain strength for samples without pre-cracks. If one then takes the horizon size to go to zero, this strength grows unbounded (Niazi et al., 2020; Stewart and Jeon, 2019). For quasi-static fracture problems, one can replace the linear-brittle bond failure model with a bilinear one (Niazi et al., 2020), which can be calibrated to both the material's fracture toughness (related to how cracks propagate, or how much energy dissipates in growing an existing crack), and its strength (related to how cracks initiate, or the peak load carried). Such a model then will initiate a crack from a rounded pit, for example, at the same peak load for any horizon size, smaller than a certain value. This could then be used to compare with experiments that monitor, at close-range, how and when cracks grow in SCC. We have, so far, not found such experiments in the literature.

In the examples we show in Sections 3 and 4, we solve both the elasticity and diffusion problems on the undeformed mechanical configuration and do not consider the effect displacements, like crack opening, for example, will have on changes in the electrolyte. This is fine as long as displacements are small. Note also that in the diffuse corrosion layer, the effect of deforming diffusion bonds is partially included via the stress/strain-dependent micro-dissolvability. The solid deformation can alter the volume of electrolyte inside corrosion pits, which further modifies the diffusion process inside liquid. Since here we assume mechanical deformations to be small, it is reasonable to ignore this effect. This is especially true for the activation-controlled corrosion cases (metal ion concentration in the liquid phase is kept constant zero) considered in Sections 3 and 4, in which mechanical deformation should have no effect on the diffusion in the electrolyte.

For the sequentially coupled mechano-corrosion-damage calculation (see Fig. 4), a proper time step (Δt) has to be selected for the transient corrosion simulation to be stable. The maximum value for the time step can be computed from the stability condition (see Oterkus et al., 2014; Silling and Askari, 2005; Zhao et al., 2018). For the simulations shown in Sections 3and 4, we test several time

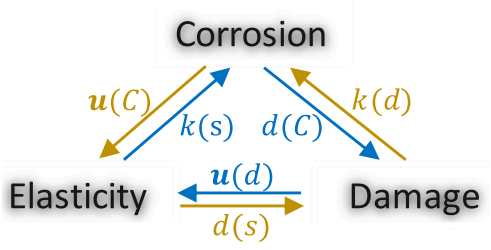

Fig. 3. Schematic of the coupled peridynamic corrosion-fracture model.

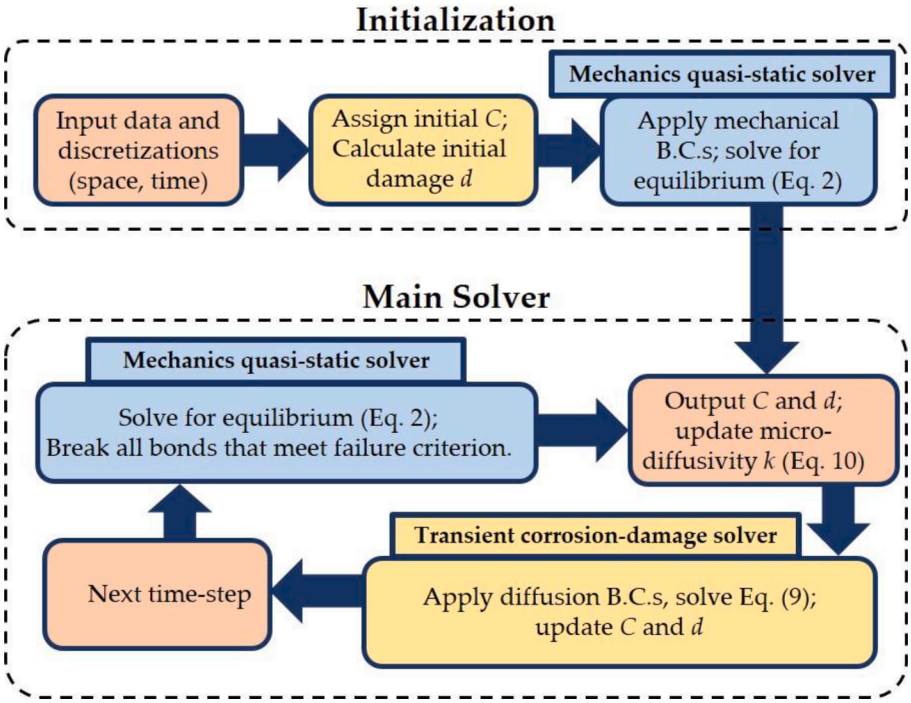

Fig. 4. Graphical illustration of the coupled stress-assisted corrosion solver.

steps to observe the effect on the coupled for the coupled model.

Since the corrosion dissolution time scale is much longer than that of crack growth, in addition to the time step (Δt) for the transient corrosion-damage calculation, we also select the interval (ΔT, a multiple of Δt) after which a solution with the mechanical solver will be initiated in the overall time-loop. The mechanical solver finds the new equilibrium conditions, updating bond strains, bond breakage, and the damage index map. A balance has to be struck between efficiency and accuracy: choosing the same value for ΔTas for Δtwill be accurate, but neither efficient nor necessary. For the selection of (ΔT), two factors need to be considered: the stress-dependence constant γ (see Eqs. (13)and (15)) and Δt. When these two values are small, and at each corrosion time step (Δt) the variation in micro-dissolvabilities is negligible, one can solve for mechanical equilibrium and update bond strains every several Δtsteps. In Sections 3and 4 we perform some convergence tests to determine a proper time interval (ΔT) for updating the mechanical field.

In the next two sections, we consider 2D and 3D SCC tests, respectively. Since SCC experiments are performed under 3D conditions in general, in Section 4 we validate the model against experimental measurements.

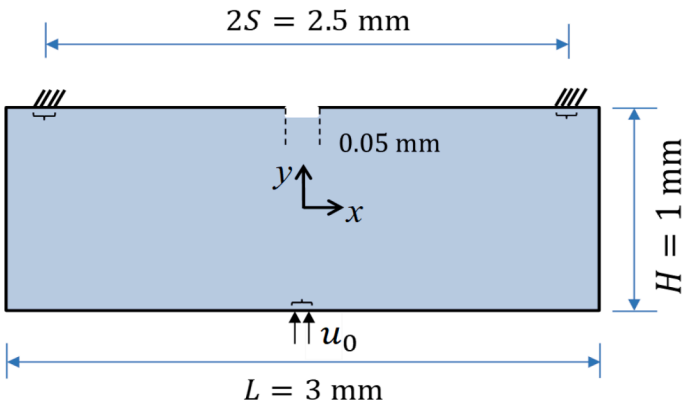

Fig. 5. Geometry and boundary conditions for 2D SCC (plane-strain conditions): a metal beam under three-point bending conditions and activation-controlled corrosion occurring through the top-center initial defect in the passive film that covers the top beam surface.

3. Combination of anodic dissolution and mechanical damage for SCC in a 2D problem

In this section, we use the new PD model to simulate SCC in a 2D beam subjected to three-point bending and corroding conditions at a pre-notch. We also show how to determine a proper time interval (ΔT) for updating the mechanical field in the coupled model. The goal is to observe how the two mechanisms, stress-dependent anodic dissolution and diffuse corrosion layer (DCL)-assisted fracture, influence crack propagation in stress corrosion cracking.

The 2D simulation setup is shown in Fig. 5. A stainless steel beam with a rectangular cross-section of 1 mm by 3 mm, is subjected to three-point bending conditions (plane-strain): two square regions of size $\delta \times \delta$on both sides of the top surface are fixed in the vertical direction, while another square region (of same dimensions) in the middle of the bottom side of the beam is displaced by $u_o = 5$ μm, and held there in time. Corrosion is allowed only at the top boundary of the beam. Initially, the beam's top surface is protected by a passive film, except for a "defect" or small pit at its middle were we manually break the passive film. To mimic the presence of a passive film in the PD model, we do not enforce any conditions on that boundary, since this is equivalent to enforcing a zero-flux condition. We implement the defect as an initial pitting damage by setting the metal ion concentration in the defect area (one layer of nodes located at the top center within the 0.05 mm segment in Fig. 5) to zero, and keep it zero for all time. The rest of the boundaries have zero flux conditions imposed. We assume a corrosion process in activation-controlled regime, similar to the actual conditions in which fresh electrolyte flushes the top surface at all times, or when the electrolyte volume is large and no diffusion-limited processes get activated.

Note that, a PD formulation usually requires associated nonlocal boundary conditions, sometimes called "volume constraints". However, there are reasons for wanting to impose local boundary conditions in a PD model (Aksoylu and Gazonas, 2020; Zhao et al., 2020). For example, measurements are normally available at the surface of a sample, not through a thick layer. There are several options for imposing local boundary conditions in PD, and some are discussed in detail in Zhao et al. (2020). In the limit of the horizon going to zero (and discretization size going to zero), they all approach the classical boundary condition. In our implementation, we choose to impose local, Dirichlet boundary conditions by fixing values on a layer of nodes, which means over a certain thickness. This is close to, but slightly different from a local boundary condition, normally enforced, at geometrical features (points/lines/areas) of zero thickness.

We assume a Young modulus value $E = 210$ GPa, and a fracture energy $G_0 = 1{,}000$ J/m^2, parameters from the 3D example shown in the next section. Although stainless steel is usually ductile and plastic deformation needs to be considered, in a corrosive environment, ductility is significantly reduced and fracture can become quasi-brittle (see e.g. Contreras et al., 2012). Because of this, here we do not consider plastic deformations and assume the fracture process to be brittle. In many cases, plastic deformation cannot be neglected and for that, the current model would need to be extended to include elasto-plastic deformations.

Here, we focus on the pit-to-crack transition and aim to qualitatively test the model's ability of capturing SCC mechanisms. The "exact" fracture behavior is of secondary importance for this purpose. We simulate crack growth due to mechanical loadings using a linear elastic and brittle fracture model, similar as the one used in Silling (2000), based on strain-induced bond breaking.

We select $C_{\text{solid}}$and $C_{\text{sat}}$to be 143 M and 5.1 M, respectively, these being typical values for stainless steel (Chen and Bobaru, 2015a). For an activation-controlled corrosion, the metal concentration in the electrolyte remains close to zero during the corrosion process. In the simulations, the electrolyte is represented by the initial boundary condition on the top surface (the defect region subject to zero metal ion concentration) and the growing pit from it. All electrolyte nodes have zero metal ion concentration imposed on them. Defects in the real passive film form due to a complex combination of material heterogeneities, loading conditions and local electrochemistry (Wei et al., 2018; Zhang et al., 2012; Zheng et al., 2013). As a pit grows from a defect, the top passive layer may also get dissolved in cases when there is no repassivation. In our model, solid nodes on the top boundary are dissolved from the sides and from underneath, as the initial pit widens and we do not simulate repassivation here.

For this generic 2D simulation the horizon size is selected to be 40 μm, which is small enough compared to the geometrical length scales and large enough to allow for relatively fast simulation times. The domain is uniformly discretized with the grid size Δxin the $x$and y directions. A grid spacing $\Delta x = 10$ μm(corresponding to $m = 4$) is used for all simulations, except for the ones in which we investigate the influence of $m$parameter. The horizon size in the current PD model represents the damage layer thickness (Jafarzadeh et al., 2018b). The corrosion damage layer is generally composed of the corrosion product layer and the diffuse corrosion layer. Its thickness can vary from less than 1 micron to several hundreds of microns (Li et al., 2016; Vallabhaneni et al., 2018; Zhang et al., 2014). It is reasonable to assume that specific profile of the damage layer affects fracture behavior, especially for thicker damage layers. We do not, however, consider this topic here.

Consistent with an activation-controlled corrosion process, we assume a relatively small corrosion rate (Chen and Bobaru, 2015a). We consider dissolvability at the corrosion front to be 0.02 μm^2/s, which leads to a value of $k^u_{\text{diss}} = 1.59\text{e-}5$ s^{-1}for the micro-dissolvability. To observe how the value of the strain-dependence constant γaffects the corrosion cracking process, in Eq. (15)we take it to be 100, 300 and 500. Note that $\gamma$for stress-assisted corrosion in copper is around 275 (Jafarzadeh et al., 2019c). For a specific material, one calibrates the micro-dissolvability of unstressed material (k^u_{diss}) and the stress-dependency coefficient (γ) via two trial simulations and two measured current densities: one each for the unstressed and stressed cases (see Jafarzadeh et al., 2019cfor the details). The time step (Δt) for the corrosion-damage diffusion-driven solver is set to 20 s.

Once the time step (Δt) for the corrosion-damage diffusion-driven solver is chosen, we obtain a proper time interval (ΔT) for updating the mechanical fields (displacements, mechanical damage) by performing a study on the relationship between $\alpha = \frac{\Delta T}{\Delta t}$and the pit-to-crack transition time. Notice that the pit-to-crack transition time we consider here is not the moment when the first bond breaks due to mechanical loading, because a single bond-break may not necessarily lead to the cascading event which results in crack growth. Instead, we define the pit-to-crack transition time as the moment when the location of maximum strain energy density changes by at

least a certain distance (chosen here to be 2δ) after a call to the mechanical solver. The mechanical solver exits when no more bonds are breaking, which can happen either when the crack arrested or when the full sample has split apart.

Fig. 6 shows the variation of the pit-to-crack transition time versus α. In this figure, the vertical line segments mark the length of the time interval ΔTused between calls of the mechanical solver. The results show that the transition time comes earlier for higher γ. This is expected since higher γtriggers faster advancement of the corrosion front in the direction of higher dilatation. This means a more elongated pit is generated, which enhances the stress concentration, which in turn makes the corrosion rate faster, in a feedback loop.

For a specific γ, the pit-to-crack transition time varies significantly with different choices of α, especially for small such values. The likely explanation for this comes from the corrosion-dependent damage (CDD) model (Chen and Bobaru, 2015a) which randomly breaks solid bonds in the damage layer based on the concentration drop at solid nodes these bonds connect. For the 2D model with $m = 4$, the maximum number of family nodes belonging to a node is less than 70 and only part of them have a node in the damage layer. A small number of such bonds would lead to higher variability on the stress field in the damage layer where the crack initiates from, and thus lead to the large variation for the transition time observed in Fig. 6. In support of this conjecture, we compute the variation of transition time relative to $\alpha$for $m = 8$ (see Fig. 6) The number of family nodes in this case is around 250. With more bonds inside the horizon, the earlier observed variability should be smaller, and this is what we indeed see.

Moreover, when α(the number of corrosion solver calls between two consecutive calls to the mechanical solver) is large, the variability of bond breaking in the CDD model is reduced by an averaging process. Therefore, larger αshould show smaller variability in terms of the pit-to-crack transition time. Notice that using a smaller αdoes not necessarily accelerate the pit-to-crack transition when $\gamma$is not large enough to dominate the effect of bond-breaking stochasticity.

For the remaining simulations in this 2D example, we choose $\alpha = 100$ ($\Delta T = 100\Delta t = 2{,}000$ s). In Fig. 7, we show the damage and dilatation maps at different times computed by the coupled corrosion/cracking model for the $\gamma = 100$case, as well as the zoom-in images of the pit for different γvalues at times just before a crack grows from the pit.

The results (see Fig. 7) show that once corrosion damage creates regions of high stress concentration, the corrosion rate, which in our model depends on local strain (dilatation), starts to increase, leading to a notch with a more elongated shape, which further increases the stress concentration factor. When the strain energy density (bond strains) at the pit's bottom becomes critical, a crack initiates and propagates, and can eventually arrest when the strain energy drops below the critical value. For a higher stress-dependency coefficient γ, the pit shape is more elongated and the pit-to-crack transition happens earlier, as one would expect. Once the crack forms, the electrolyte will fill the crack opening and corrosion will continue. For a large enough structure, such a mechanism may repeat as a "stop and go" mode, with anodic dissolution-damage and mechanical damage alternating in advancing the crack. In our current model, however, we do not take this into account.

SCC is generally attributed to one of two groups of mechanisms (Winzer et al., 2005): anodic dissolution or cleavage. For the dissolution mechanism, in its simplest form, dissolution at a film-free crack tip causes crack advancement. The cleavage mechanism includes: (1) an embrittled region forming ahead of the crack tip, (2) crack growth through the embrittled region, and (3) crack arresting as it enters the more ductile bulk material. The results shown in Fig. 7 indicate how SCC can progress from a combination of the two possible mechanisms modeled here: anodic dissolution and mechanical damage. Note that in our simulations, since the material is treated as brittle, once the strain-induced crack starts to grow, it grows over a significant length before arresting due to the relaxation in strain energy density. In some cases, one would expect cracks to run only a short distance before arresting due to plastic deformations. Note also that, in certain metallic materials, repassivation can take place (a passive film reforms due to the local chemistry at the corrosion front) and affect the anodic dissolution. This is not yet considered in the present model. However, repassivation mechanisms have been introduced in PD models of corrosion (Jafarzadeh et al., 2018b; Jafarzadeh et al., 2019a).

In this example, if we had set the bending deformation to be smaller, we would have only seen pitting corrosion. Vice-versa, had we

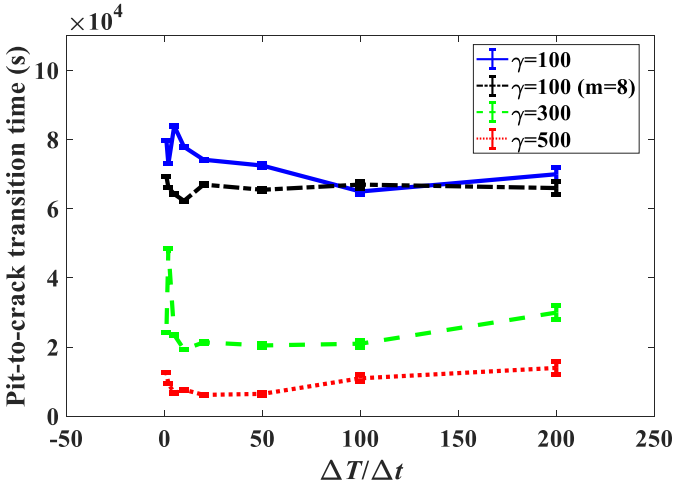

Fig. 6. The influence of $\alpha = \Delta T/\Delta t$and the stress-dependency coefficient γon the pit-to-crack transition time.

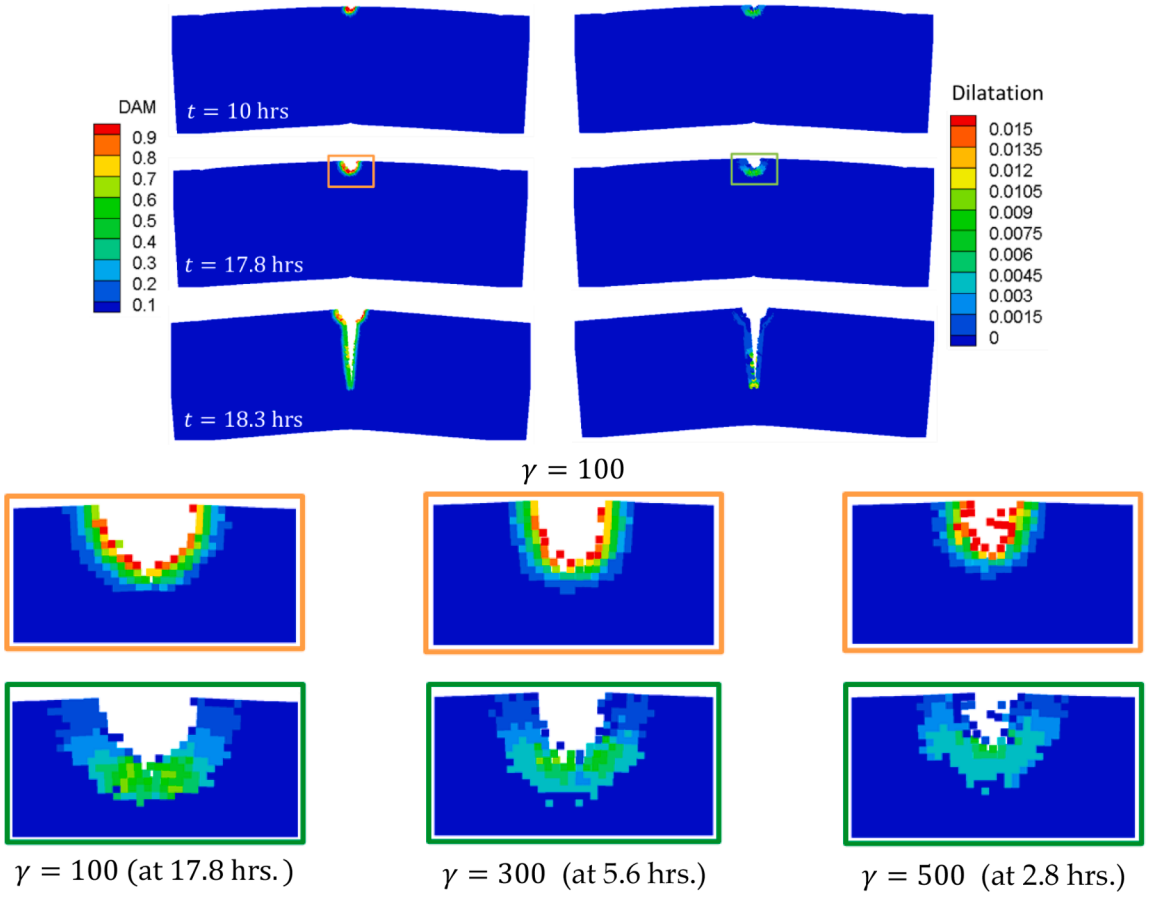

Fig. 7. Top section: evolution of anodic dissolution damage and crack growth (left) and contours of mechanical dilatation (see Eq. (15)) (right), for the three-point bending example in Fig. 5, with $\gamma = 100$and $\alpha = 100$. Bottom section: details around the pits comparing damage maps (top row) and corresponding dilatation (bottom row) for different values of γat times slightly before a crack is initiated. In all plots, displacements are magnified 10 times.

imposed a larger displacement of the beam in three-point bending, we would have obtained a crack that would have initiated earlier, and could have fully fractured the sample.

Because there are no 2D SCC experiments that we could validate these simulation results with, in the next section we perform a validation test in 3D for which experimental measurements are available in terms of the pits morphology evolution and the pit-to-crack transition time.

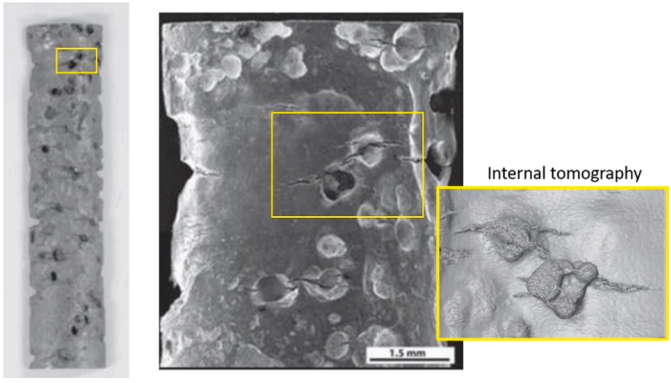

Fig. 8. The 3NiCrMoV steam turbine disc steel specimen after 7173 h in aerated water with 1.5 ppm Cl^- and at 90° C. Left side: photo of the whole specimen; center: SEM image of a portion of the sample; right: internal tomogram of two pits and cracks (from (Horner et al., 2011)).

4. Validation of the coupled PD model for SCC in 3D

In this section we use the coupled PD model for a 3D simulation of SCC in a type of steam turbine steel exposed to hot aerated water. The experimental setup and data are taken from Ref. Horner et al. (2011), where detailed characterization and mechanical and chemical parameters were given for the tensile loading of a bar exposed to a corrosive environment for months. We give brief descriptions of the experiment and the PD model setup. We then compare our results with those from the experiment. The objective of our validation test is to predict the damage patterns (pits' morphology, microcracks).

4.1. Brief review of the experiment in Horner et al. (2011)

A cylindrical specimen made of 3NiCrMoV steam turbine disc steel, with yield stress $\sigma_Y = 705$ MPa, is loaded by an axial tension 90% of σ_Y(Horner et al., 2011). The loaded specimen is immersed in aerated water with 1.5 ppm $Cl^-$and 90 °C temperature (Horner et al., 2011). After about 10 months (7173 h) under these conditions, the corroded specimen, which also presents several micro-cracks, looks as in Fig. 8 below, taken from Horner et al. (2011).

Fig. 8 shows randomly distributed pits all around the surface of the corroded steel bar, as well as some cracks that appear to start from these pits or connect them. Note the variety of pit sizes and depths, which implies that pits likely did not initiate simultaneously. In the present work, we focus on the growth of two neighboring corrosion pits from which cracks have initiated (see the frame in Fig. 8), and the transition from pitting to cracking, under the tensile loading condition. Since these two pits are of similar size, in the simulation shown in what follows we assume that they initiate simultaneously.

Initiation of corrosion pits is related to the detailed electrochemistry of the passive layer breakdown and the mechanical loading conditions. Several models are available for the initiation phase of pitting corrosion (Bargeron and Givens, 1980; Macdonald, 1992; McCafferty, 2003), but are not included in the present study, where we assume that the pits start from some existing micro-pits.

4.2. Computational model setup

To reduce the computational size of model, we limit our simulation to a small cuboid $2 \times 2 \times 1$ mm^3near the surface of the steel rod. This simplification means that our simulation is only an approximate one, since we apply constant mechanical boundary conditions to this small part of the bar. In reality, as pits grow and cracks initiate, the loading conditions on the cuboid vary in time. However, such an approximation should be a close one, at least up to the point when major cracks form. Boundary conditions for the corrosion process involve only the top surface of the cuboid, corresponding to the rod surface. Zero-flux conditions are imposed on all other surfaces.

Two initial hemispheric micro-pits/defects with radii of 80 μmare placed on the top surface in Fig. 9. The locations of these micro-pits as initiation sites are chosen by estimating the centers of the experimental pits shown in Fig. 8and how they are aligned with respect to each other and the loading direction. The domain is under uniaxial tension with fixed imposed displacements applied, at all times, on the two opposite side surfaces (parallel to yz-plane in Fig. 9). Fig. 9 schematically shows the computational model geometry and boundary conditions.

To reach the normal stress as applied in the experiment (of 90%$\sigma_Y$along the x-direction), we need to apply a displacement of $\Delta u = 3.02$ μmon both sides of the computational cuboid sample in Fig. 9, given that the Young modulus for this material is 210 GPa. The rest of the surfaces are considered to be traction free, which is an approximation of the real conditions. The fracture energy (G_o) for this material in this specific severe environment is not available in the literature. We set $G_o$to be 1,000 J/m^2. The stress corrosion cracking critical stress intensity factor (K_{ISCC}) for a similar alloy in similar, but not identical, harsh environments is reported to vary between ~15 to 30 MPa.$m^{1/2}$, depending on the environmental specifics (McMinn et al., 1985). According to the relationship $G_0 =$

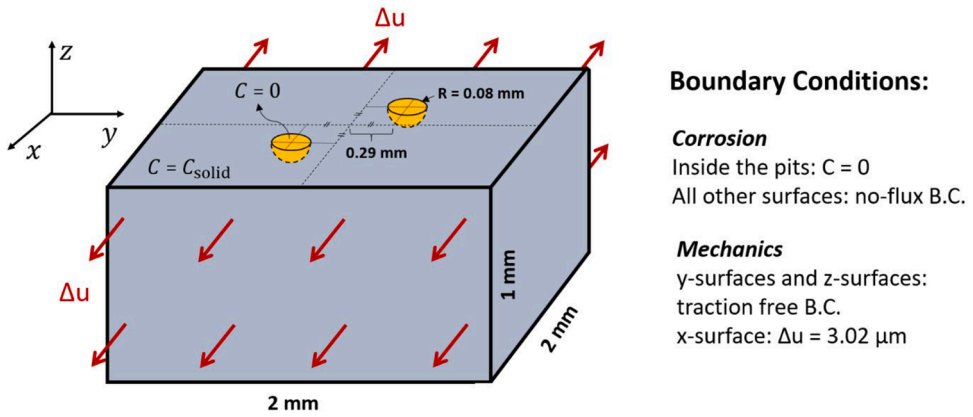

Fig. 9. Computational domain and initial and boundary conditions for the 3D example.

$\frac{K_{IC}^2}{E}$(Anderson, 2017), the assumption of $G_o = 1{,}000$ J/m^{2}is equivalent to K_{ISCC} =14.5 MPa $\cdot$ m$^{1/2}$, which is close to the minimum of the range reported in McMinn et al.(1985).

As in the 2D example in Section 3, $C_{solid}$and $C_{sat}$are chosen to be 143 M and 5.1 M, typical values for stainless steel (Chen and Bobaru, 2015a). Note that we aim for a qualitative comparison, thus the exactness of $C_{solid}$and C_{sat}values is of secondary importance. The initial concentration value, and at all times, is set to zero inside the initial pits. This is a good approximation for activation-controlled corrosion, when the sample is continuously flushed by fresh electrolyte, or when the dissolution rate is much slower than the diffusion in the electrolyte, which is the case in the experiments considered here. We set the concentration to $C_{solid}$for the rest of the domain, initially. No-flux boundary conditions are assumed for the remaining surfaces. These conditions are similar to the assumptions made for the 2D example.

For this simulation the horizon size is selected to be 80 μm, which is the scale of the initial micro-pits, and large enough to be efficient. The domain is uniformly discretized with a grid size $\Delta x = 20$ μmin x, y, and z directions.

According to the experimental measurements in Horner et al. (2011), the average pit growth rate is 1.22e-5 μm $\cdot$ s^{-1}. We calibrate the micro-dissolvabilty to this value and obtain k_{diss} = 9.48e-4 m^{-1}s^{-1}. For calibration details see Jafarzadeh et al.(2019c). The stress-dependence constant γrepresents the degree of influence of stress on the corrosion rate. Therefore, in the simulation, pit's shape is influenced by γ. In reality, pit shape also depends on material heterogeneity, convection in the liquid, surrounding pitting evolution, etc. The experimental value for $\gamma$for this alloy is not available. An experimental and analytical procedure to obtain this parameter for a particular material is reported in Jafarzadeh et al. (2019c). For this example, we select several γ values: 5100, and 300, respectively, to find whether any leads to results (pit-to crack transition time, and pit/crack morphology) similar to what is experimentally observed in Horner et al. (2011).

We note that the provided experimental rate of pit growth is an averaged value for 10 months of immersion. The times when the pits initiate from the surface are not given in Horner et al. (2011), but other experiments show that pitting may start as soon as the immersion (Ghahari, 2012). The pits we selected from the pictures in Fig. 8 to simulate are some of the deepest, meaning that they likely started at, or soon after, immersion. In the peridynamic model we assume that pitting starts at the beginning of the simulation from the two existing micro-pits.

4.3. Results and discussion

For a numerically stable solution, we set the time step (Δt) for the corrosion-damage solver to be 44 h. Similar to the 2D case in Section 3, we investigate the variation of the pit-to-crack transition time to the time interval (ΔT) for updating the mechanical fields. The results are shown in Fig. 10where six ΔTintervals are used: 2200 (50Δt), 880 (20Δt), 440 (10Δt), 220 (5Δt), 88 (2Δt), and 44 (1Δt) h., respectively. Due to the higher computational cost than in 2D, the 3D simulations are performed on a *Tesla V100 GPU (16 GB Card)*, using an in-house Fortran 90 computer program parallelized by OpenACC. With this code, it takes about 2 h. (for the case $\Delta T = 5\Delta t$) to simulate 11,000 h. of actual corrosion time. The vertical line segments in Fig. 10represent the time ranges during which the first crack forms. The length of each line segment corresponds to the value of the time interval ΔTused.

Similar to the 2D case (see Fig. 6), larger γleads to earlier pit-to-crack transition times, as expected. Interestingly, different from the 2D case (see Fig. 6), the results for the 3D case show that the pit-to-crack transition time stabilizes to around 9400, 6700 and 3240 h, for $\gamma = 5{,}100$ and 300, respectively (see Fig. 10). As discussed in Section 3, one possible explanation for this behavior has to do with the embedded stochasticity in the corrosion-dependent damage model (Chen and Bobaru, 2015a). In our SCC model, crack initiation is related to the mechanical loading condition, corrosion-induced morphological change (stress concentration), and the diffuse corrosion layer (DCL) which possesses stochastically-generated graded mechanical damage (Chen and Bobaru, 2015a; Jafarzadeh et al., 2018b; Li et al., 2016). In the early stages of the 2D example, the crack initiates while the pit is still very small (relative to the horizon size). Therefore, the effect of damage stochasticity in the DCL, whose thickness is δ, on crack initiation time is high. In the 3D example, a

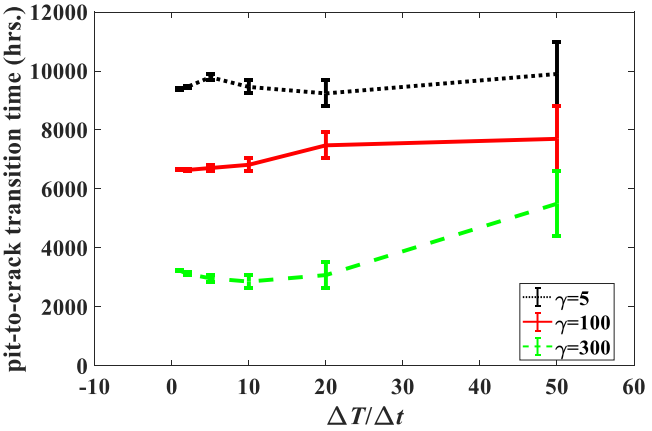

Fig. 10. The pit-to-crack transition times for different $\Delta T/\Delta t$and different stress-dependency values γ.

Fig. 11. The influence of stress-dependency coefficient γon the corrosion cracking pattern. Bird-views (upper row) and perspective view (bottom row). The loading directions are indicated by the arrows.

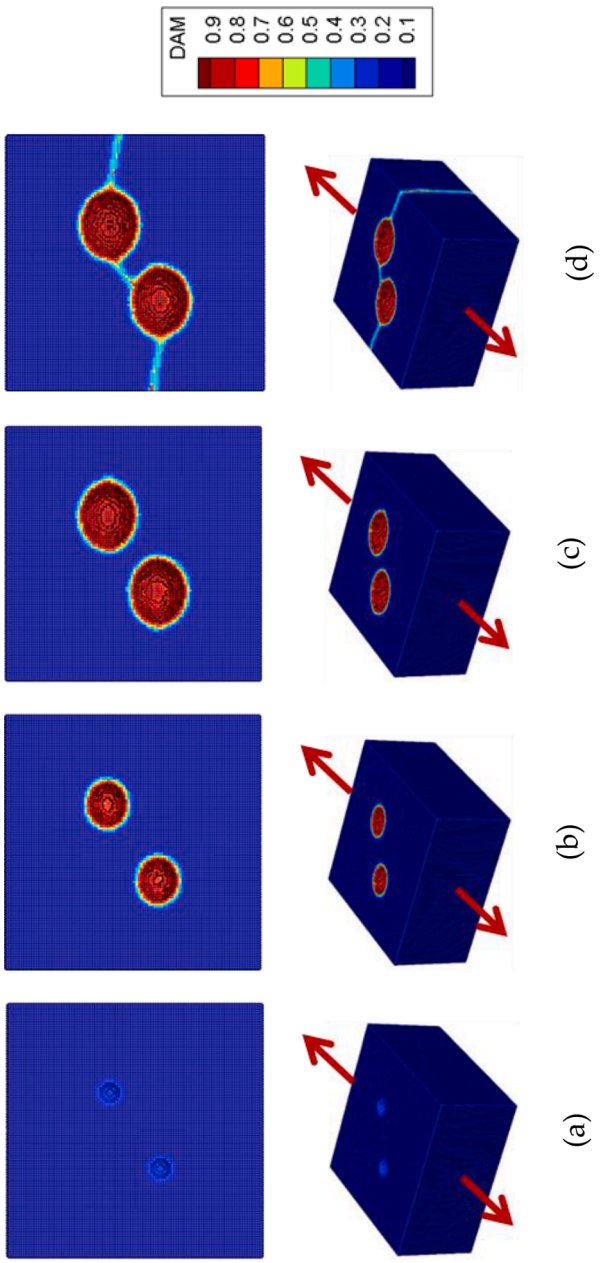

Fig. 12. Time-evolution for damage maps from peridynamic simulation of SCC at the (a) initial stage, and at (b) 4400 h, (c) 6600 h, (d) 6688 h. of immersion. Top row shows the top view and the loading directions are indicated by the arrows.

crack initiates when the pit is much larger than the horizon size. This reduces the influence of DCL stochasticity on crack initiation. Moreover, for a horizon factor $\frac{\delta}{\Delta x} = m = 4$, in 3D a node has about 400 neighbors, while in 2D only about 70. The sensitivity to stochastic bond-breaking, whenever corrosion damage increases, is thus higher in 2D examples than in 3D ones.

We also notice that, unlike the 2D case, the variation of the transition time for smaller $\alpha$is not larger than that for larger α. The likely reason is that for the 2D three-point bending problem, only a few nodes located at the pit bottom determine crack initiation, which adds extra sensitivity to the frequency of calls to the mechanical solver, especially for a small αvalue. In the 3D case, however, crack initiation is determined by many more nodes at the pit bottom, averaging the effect of stochasticity. Therefore, the intrinsic stochasticity in the PD corrosion model has less of an effect when $\alpha$is small, in the 3D case.

Based on the results shown in Fig. 10, we choose to use $\alpha = \frac{\Delta T}{\Delta t} = 2$(even though a value as high as 10 would also work) for our investigation of the 3D SCC problem.

The influence of γon the pit morphology at the pit-to-crack transition time and the corresponding fracture patterns are shown in Fig. 11. As expected, we observe that higher γvalues lead to more elliptical pits shape (see Fig. 11), which produce higher stress-concentration and earlier pit-to-crack transition times (see Fig. 10). The elongations are according to the applied loading.

Since the pit-to-crack transition time for $\gamma = 100$is nearest the experimental measurements from Horner et al. (2011), we investigate the time evolution of the SCC process using this value and compare the simulated pit morphology and corrosion cracking patterns to the experimental observations.

The time evolution of the SCC process is shown in Fig. 12. We observe that the pits grow slightly elliptical, more elongated in the direction perpendicular to the applied load direction, as regions with higher stress/strain concentrations corrode at a faster rate. At some point, fracture occurs suddenly with cracks initiating from both pits and one joining the pits (see Fig. 12c). It is interesting to notice that a crack joining the pits is also observed in the experiments (see Fig. 8). The entire sample is split, given that we do not model the entire steel rod, but only the small cube and with the simplified boundary conditions shown in Fig. 9. Video 1 shows this evolution over 6688 h. of exposure to tension and corrosive conditions.

Video 2 shows the 3D internal damage time evolution obtained by the new PD model for SCC. Fig. 13 shows the internal damage profile (pits and cracks) from three different direction views at 6688 h. of exposure.

The simulated damage profile at 6688 h. (when cracking occurs) is compared with the experimental observations in Fig. 14.

The computed pits' size and shapes as well as the morphology of cracks that spring from the two pits or connect them, are very similar to those observed experimentally in Horner et al. (2011). We can conclude that the SCC mechanisms implemented in our coupled model may be sufficient to explain, to first order, the observed phenomenon. We also note that, in the experiment, the cracks are arrested. In our simulation, they propagate and fully split the modeled small cuboid. One reason for this is that the material model we employed was a brittle fracture one. In the actual turbine steel, small plastic deformations can arrest a growing crack. Moreover, the resulting stress distribution from our simplified BCs (fixed displacement controlled) is not identical to the stress field produced in the loaded cylindrical specimen with pits growing on its surface, especially once cracks start growing.

The comparison of our simulation results with experimental ones can be viewed as a "qualitative" validation. In absence of a measured value for the fracture energy under the imposed corrosive conditions, we used an educated guess. Also missing from the experimental literature was the corrosion rate stress-dependency for the particular steel: we selected that parameter such that the crack-to-pit transition time was consistent with the experimental observations. However, once those values were set, the model was able to reproduce/validate with high fidelity the size of the pits at the pit-to-crack transition time, as well as the crack patterns for the cracks springing from or joining the two pits, even as we considered simplifying boundary conditions to reduce the high computational cost modeling of the entire sample would have required.

From the point of view of damage morphology (pits and cracks), we can consider this example a "quantitative" validation because various other scenarios could have been possible, such as: cracking could have occurred earlier, when pits were smaller, or cracks could

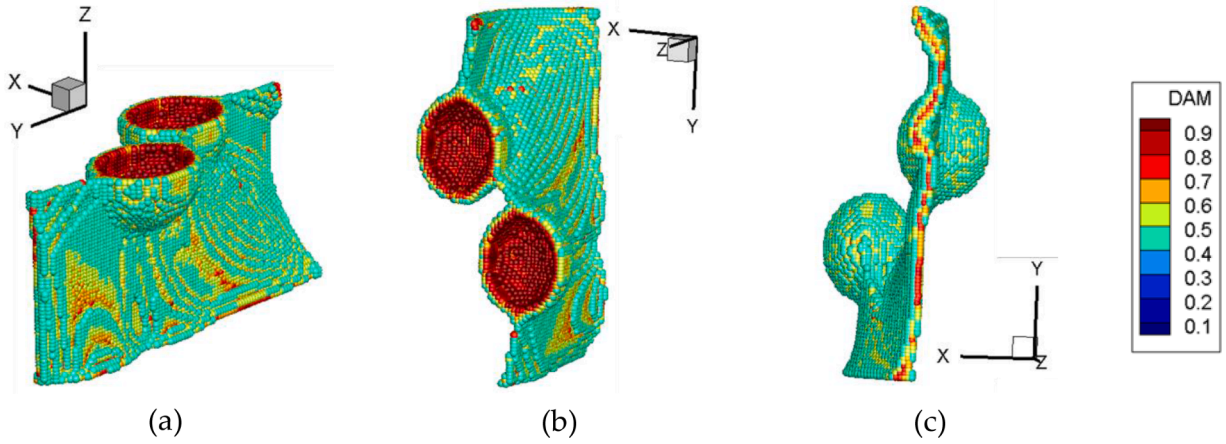

Fig. 13. Internal damage (pits and crack) from PD-computed SCC, viewed from different directions. Nodes with zero damage are not shown.

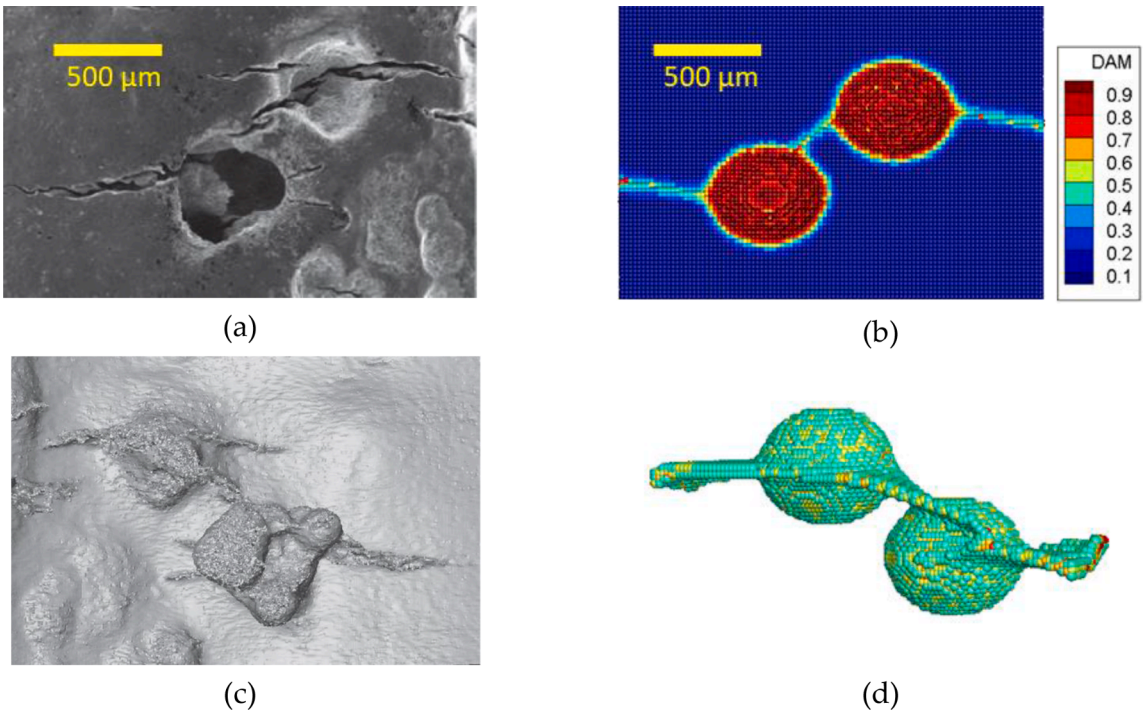

Fig. 14. Pits and cracks: experimental results (a and c, after 7173 h. exposure; from Horner et al., 2011) and PD-computed results (b and d, at 6688 h. exposure). (a): SEM image of the sample surface; (b) top view for PD-computed damage map; (c) back-side tomogram of experimental pits and cracks; (d) back-side view of PD-computed damage (part of the crack deep surface is cut for a better view of the pits' back side morphology and the crack linking them).

have grown from one of the pits only; or pits could have grown and merged before cracks initiated. The fact that the model captures well the morphology seen from experiments gives us confidence that the parameters used for the fracture energy and the stress-dependency of the corrosion rate are likely close to the real values. We are eagerly waiting for experimental confirmation of this conjecture from the readers.

This example shows the capability of our peridynamic SCC model in simulating complex mechano-chemical SCC in 3D, in a unified framework.

5. Conclusions

We introduced a mechano-chemical peridynamic model to simulate stress-corrosion cracking (SCC). A new bond-failure criterion extends our previous stress-assisted corrosion model and allows damage caused by mechanical strains. The coupled model is capable of simulating a seamless transition between the evolving corrosion process and autonomous crack growth. An example of cracks originating from pits that grow in a steel (steam turbine steel) rod subjected to tensile loading and exposed to a corrosive environment for months was used to validate the model.

The new peridynamic SCC model has the following features: (1) a unified framework is established for stress-dependent anodic dissolution and diffuse corrosion layer-assisted fracture; (2) propagation of damage is autonomous and explicit tracking of the corrosion front is not necessary; (3) the diffuse corrosion layer with degraded mechanical properties is automatically captured as part of the solution method; (4) embedded stochasticity leads to some micro-level surface roughness of pits, which can be enhanced by inserting material heterogeneities; and (5) dependency of corrosion rate on elastic deformation is taken into account.

The peridynamic model presented here for simulating SCC is highly flexible and can describe arbitrary damage configurations caused by coupled chemo-mechanical environmental/loading conditions, which is an important advantage of the approach.

Declaration of Competing Interest

None.

Acknowledgments

Z.C. acknowledges the support from the Natural Science Foundation of China (No. 11802098) and the Natural Science Foundation

of Hubei Province (No. 2018CFB111). The work of the rest of the authors has been supported by the ONR project #N00014-15-1-2034 "SCC: the importance of damage evolution in the layer affected by corrosion" (program manager William Nickerson), the AFOSR MURI Center for Materials Failure Prediction through Peridynamics, by the National Science Foundation under CMMI award No. 1953346, and by a Nebraska System Science award from the Nebraska Research Initiative. The computations have been performed utilizing the Holland Computing Center of the University of Nebraska, which receives support from the Nebraska Research Initiative.

Supplementary materials

Supplementary material associated with this article can be found, in the online version, at doi:10.1016/j.jmps.2020.104203.

References

Aksoylu, B., Gazonas, G.A., 2020. On nonlocal problems with inhomogeneous local boundary conditions. J. Peridyna. Nonlocal Model. 2, 1–25.
Anderson, T.L., 2017. Fracture Mechanics: Fundamentals and Applications. CRC Press.
Ansari, T.Q., Xiao, Z., Hu, S., Li, Y., Luo, J.-L., Shi, S.-Q., 2018. Phase-field model of pitting corrosion kinetics in metallic materials. NPJ Comput. Mater. 4, 38.
Badwe, N., Chen, X., Schreiber, D.K., Olszta, M.J., Overman, N.R., Karasz, E.K., Tse, A.Y., Bruemmer, S.M., Sieradzki, K., 2018. Decoupling the role of stress and corrosion in the intergranular cracking of noble-metal alloys. Nat. Mater. 17, 887–893.
Bargeron, C.B., Givens, R.B., 1980. Precursive blistering in the localized corrosion of aluminum. Corrosion 36, 618–625.
Bobaru, F., Duangpanya, M., 2010. The peridynamic formulation for transient heat conduction. Int. J. Heat Mass Transf. 53, 4047–4059.
Bobaru, F., Duangpanya, M., 2012. A peridynamic formulation for transient heat conduction in bodies with evolving discontinuities. J. Comput. Phys. 231, 2764–2785.
Bobaru, F., Foster, J., Geubelle, P., Silling, S.A. (Eds.), 2016. Handbook of Peridynamic Modeling. CRC Press.
Chadwick, A.F., Stewart, J.A., Enrique, R.A., Du, S., Thornton, K., 2018. Numerical modeling of localized corrosion using phase-field and smoothed boundary methods. J. Electrochem. Soc. 165, C633–C646.
Chen, Z., Bobaru, F., 2015a. Peridynamic modeling of pitting corrosion damage. J. Mech. Phys. Solids 78, 352–381.
Chen, Z., Bobaru, F., 2015b. Selecting the kernel in a peridynamic formulation: A study for transient heat diffusion. Comput. Phys. Commun. 197, 51–60.
Chen, Z., Zhang, G., Bobaru, F., 2016a. The influence of passive film damage on pitting corrosion. J. Electrochem. Soc. 163, C19–C24.
Chen, Z.G., Bakenhus, D., Bobaru, F., 2016b. A constructive peridynamic kernel for elasticity. Comput. Meth. Appl. Mech. Eng. 311, 356–373.
Cheng, Z., Fu, Z., Zhang, Y., Wu, H., 2020. A peridynamic model for analyzing fracture behavior of functionally graded materials used as an interlayer. Acta Mech. Solida Sin. 1–12.
Connolly, B.J., Horner, D.A., Fox, S.J., Davenport, A.J., Padovani, C., Zhou, S., Turnbull, A., Preuss, M., Stevens, N.P., Marrow, T.J., Buffiere, J.Y., Boller, E., Groso, A., Stampanoni, M., 2006. X-ray microtomography studies of localised corrosion and transitions to stress corrosion cracking. Mater. Sci. Technol. 22, 1076–1085.
Contreras, A., Hernandez, S.L., Orozco-Cruz, R., Galvan-Martinez, R., 2012. Mechanical and environmental effects on stress corrosion cracking of low carbon pipeline steel in a soil solution. Mater. Design 35, 281–289.
Cramer, S.D., Covino, B.S. (Eds.), 2003. ASM Handbook Volume 13A: Corrosion: Fundamentals, Testing, and Protection. ASM International.
De Meo, D., Oterkus, E., 2017. Finite element implementation of a peridynamic pitting corrosion damage model. Ocean Eng. 135, 76–83.
Di Caprio, D., Vautrin-Ul, C., Stafiej, J., Saunier, J., Chaussé, A., Féron, D., Badiali, J., 2011. Morphology of corroded surfaces: contribution of cellular automaton modelling. Corros. Sci. 53, 418–425.
Ghahari, S.M., 2012. In Situ Synchrotron X-ray Characterisation and Modelling of Pitting Corrosion of Stainless Steel. University of Birmingham.
Gutman, E.M., 1994. Mechanochemistry of Solid Surfaces. World Scientific Publishing Company.
Ha, Y.D., Bobaru, F., 2011. Characteristics of dynamic brittle fracture captured with peridynamics. Eng. Fract. Mech. 78, 1156–1168.
Hinds, G., Wickstrom, L., Mingard, K., Turnbull, A., 2013. Impact of surface condition on sulphide stress corrosion cracking of 316L stainless steel. Corros. Sci. 71, 43–52.
Horner, D., Connolly, B., Zhou, S., Crocker, L., Turnbull, A., 2011. Novel images of the evolution of stress corrosion cracks from corrosion pits. Corros. Sci. 53, 3466–3485.
Hu, W.K., Ha, Y.D., Bobaru, F., 2012. Peridynamic model for dynamic fracture in unidirectional fiber-reinforced composites. Comput. Meth. Appl. Mech. Eng. 217, 247–261.
Hu, W.K., Wang, Y.N., Yu, J., Yen, C.F., Bobaru, F., 2013. Impact damage on a thin glass plate with a thin polycarbonate backing. Int. J. Impact Eng. 62, 152–165.
Jafarzadeh, S., Chen, Z., Bobaru, F., 2018a. Peridynamic modeling of intergranular corrosion damage. J. Electrochem. Soc. 165, C362–C374.
Jafarzadeh, S., Chen, Z., Bobaru, F., 2018b. Peridynamic modeling of repassivation in pitting corrosion of stainless steel. Corrosion 74, 393–414.
Jafarzadeh, S., Chen, Z., Zhao, J., Bobaru, F., 2019a. Pitting, lacy covers, and pit merger in stainless steel: 3D peridynamic models. Corros. Sci. 150, 17–31.
Jafarzadeh, S., Chen, Z.G., Bobaru, F., 2019b. Computational modeling of pitting corrosion. Corros. Rev. 37, 419–439.
Jafarzadeh, S., Chen, Z.G., Li, S.M., Bobaru, F., 2019c. A peridynamic mechano-chemical damage model for stress-assisted corrosion. Electrochim. Acta 323, 134795.
Kondo, Y., 1989. Prediction of fatigue crack initiation life based on pit growth. Corrosion 45, 7–11.
Li, S., Chen, Z., Tan, L., Bobaru, F., 2018. Corrosion-induced embrittlement in ZK60A Mg alloy. Mater. Sci. Eng. A 713, 7–17.
Li, S., Chen, Z., Wang, F., Cui, B., Tan, L., Bobaru, F., 2016. Analysis of corrosion-induced diffusion layer in ZK60A magnesium alloy. J. Electrochem. Soc. 163, C784–C790.
Liu, Z., Li, X., Du, C., Zhai, G., Cheng, Y., 2008. Stress corrosion cracking behavior of X70 pipe steel in an acidic soil environment. Corros. Sci. 50, 2251–2257.
Macdonald, D.D., 1992. The Point-Defect Model for the Passive State. J. Electrochem. Soc. 139, 3434–3449.
Mai, W., Soghrati, S., 2018. New phase field model for simulating galvanic and pitting corrosion processes. Electrochim. Acta 260, 290–304.
Mai, W., Soghrati, S., Buchheit, R.G., 2016. A phase field model for simulating the pitting corrosion. Corros. Sci. 110, 157–166.
Malki, B., Baroux, B., 2005. Computer simulation of the corrosion pit growth. Corros. Sci. 47, 171–182.
McCafferty, E., 2003. Sequence of steps in the pitting of aluminum by chloride ions. Corros. Sci. 45, 1421–1438.
McMinn, A., Lyle Jr, F., Leverant, G., 1985. Stress corrosion crack growth in NiCrMoV turbine disc steels. Corrosion 41, 493–503.
Mehrmashhadi, J., Chen, Z.G., Zhao, J.M., Bobaru, F., 2019. A stochastically homogenized peridynamic model for intraply fracture in fiber-reinforced composites. Compos. Sci. Technol. 182, 107770.
Nguyen, T.T., Bolivar, J., Shi, Y., Réthoré, J., King, A., Fregonese, M., Adrien, J., Buffiere, J., Baietto, M., 2018. A phase field method for modeling anodic dissolution induced stress corrosion crack propagation. Corros. Sci. 132, 146–160.
Niazi, S., Chen, Z., Bobaru, F., 2020. Crack nucleation in brittle and quasi-brittle materials: A peridynamic analysis. engrXiv DOI: 10.31224/osf.io/7z8qr.
Oterkus, S., Madenci, E., Agwai, A., 2014. Peridynamic thermal diffusion. J. Comput. Phys. 265, 71–96.
Pérez-Brokate, C.F., di Caprio, D., Féron, D., de Lamare, J., Chaussé, A., 2016. Three dimensional discrete stochastic model of occluded corrosion cell. Corros. Sci. 111, 230–241.
Rusyn, B., Tors'ka, R., Pokhmurs'kyi, A.Y., 2015. Modeling of the evolution of corrosion pitting with the use of cellular automata. Mater. Sci. 50, 706–713.

Scheiner, S., Hellmich, C., 2007. Stable pitting corrosion of stainless steel as diffusion-controlled dissolution process with a sharp moving electrode boundary. Corros. Sci. 49, 319–346.
Scheiner, S., Hellmich, C., 2009. Finite volume model for diffusion-and activation-controlled pitting corrosion of stainless steel. Comput. Meth. Appl. Mech. Eng. 198, 2898–2910.
Silling, S.A., 2000. Reformulation of elasticity theory for discontinuities and long-range forces. J. Mech. Phys. Solids 48, 175–209.
Silling, S.A., Askari, E., 2005. A meshfree method based on the peridynamic model of solid mechanics. Computers & Structures 83, 1526–1535.
Silling, S.A., Bobaru, F., 2005. Peridynamic modeling of membranes and fibers. Int. J. Non Linear Mech. 40, 395–409.
Song, R., Blawert, C., Dietzel, W., Atrens, A., 2005. A study on stress corrosion cracking and hydrogen embrittlement of AZ31 magnesium alloy. Mater. Sci. Eng. A 399, 308–317.
Stafiej, J., di Caprio, D., Bartosik, Ł., 2013. Corrosion-passivation processes in a cellular automata based simulation study. J. Supercomput. 65, 697–709.
Stewart, R.J., Jeon, B., 2019. Decoupling strength and grid resolution in peridynamic theory. J. Peridynam. Nonlocal Model. 1, 97–106.
Tsuyuki, C., Yamanaka, A., Ogimoto, Y., 2018. Phase-field modeling for pH-dependent general and pitting corrosion of iron. Sci. Rep. 8, 12777.
Turnbull, A., Wright, L., Crocker, L., 2010. New insight into the pit-to-crack transition from finite element analysis of the stress and strain distribution around a corrosion pit. Corros. Sci. 52, 1492–1498.
Vallabhaneni, R., Stannard, T.J., Kaira, C.S., Chawla, N., 2018. 3D X-ray microtomography and mechanical characterization of corrosion - induced damage in 7075 aluminium (Al) alloys. Corros. Sci. 139, 97–113.
Van der Weeën, P., Zimer, A.M., Pereira, E.C., Mascaro, L.H., Bruno, O.M., De Baets, B., 2014. Modeling pitting corrosion by means of a 3D discrete stochastic model. Corros. Sci. 82, 133–144.
Wei, J.Q., Zhou, B.Q., Wan, T., Liu, K., Gong, S.K., Wu, J.J., Xu, S., 2018. Effect of Sulfate and Chloride Ions on Pitting Corrosion Behavior of 2Cr12MoV Steel at pH 6 and 90 degrees C. Int. J. Electrochem. Sci. 13, 11596–11606.
Winzer, N., Atrens, A., Song, G.L., Ghali, E., Dietzel, W., Kainer, K.U., Hort, N., Blawert, C., 2005. A critical review of the stress corrosion cracking (SCC) of magnesium alloys. Adv. Eng. Mater. 7, 659–693.
Xiang, L.H., Wei, X.S., Chen, S.Y., 2019. Numerical investigation on the stress corrosion cracking of FV520B based on the cohesive zone model. Results Phys. 12, 118–123.
Yavas, D., Mishra, P., Alshehri, A., Shrotriya, P., Hebert, K.R., Bastawros, A.F., 2018. Nanoindentation study of corrosion-induced grain boundary degradation in a pipeline steel. Electrochem. Commun. 88, 88–92.
Zhang, G.F., Le, Q., Loghin, A., Subramaniyan, A., Bobaru, F., 2016. Validation of a peridynamic model for fatigue cracking. Eng. Fract. Mech. 162, 76–94.
Zhang, X., Yang, S.W., Zhang, W.H., Guo, H., He, X.L., 2014. Influence of outer rust layers on corrosion of carbon steel and weathering steel during wet-dry cycles. Corros. Sci. 82, 165–172.
Zhang, Y., Urquidi-Macdonald, M., Engelhardt, G.R., Macdonald, D.D., 2012. Development of localized corrosion damage on low pressure turbine disks and blades: I. Passivity. Electrochim. Acta 69, 1–11.
Zhao, J., Jafarzadeh, S., Chen, Z., Bobaru, F., 2020. An algorithm for imposing local boundary conditions in peridynamic models on arbitrary domains. engrXiv DOI: 10.31224/osf.io/7z8qr.
Zhao, J.M., Chen, Z.G., Mehrmashhadi, J., Bobaru, F., 2018. Construction of a peridynamic model for transient advection-diffusion problems. Int. J. Heat Mass Transf. 126, 1253–1266.
Zheng, S.Q., Li, C.Y., Qi, Y.M., Chen, L.Q., Chen, C.F., 2013. Mechanism of (Mg,Al,Ca)-oxide inclusion-induced pitting corrosion in 316L stainless steel exposed to sulphur environments containing chloride ion. Corros. Sci. 67, 20–31.
Zhu, L.K.K., Yan, Y., Qiao, L.J.J., Volinsky, A.A., 2013. Stainless steel pitting and early-stage stress corrosion cracking under ultra-low elastic load. Corros. Sci. 77, 360–368.